ExoMoL line lists – XXIX. The rotation-vibration spectrum of methyl chloride up to 1200 K

A. Owens,[1,2]★ A. Yachmenev,[1,2] W. Thiel,[3] A. Fateev,[4]
J. Tennyson[5]★ and S. N. Yurchenko[5]★

[1]*The Hamburg Center for Ultrafast Imaging, Universität Hamburg, Luruper Chaussee 149, D-22761 Hamburg, Germany*
[2]*Center for Free-Electron Laser Science (CFEL), Deutsches Elektronen-Synchrotron DESY, Notkestrasse 85, D-22607 Hamburg, Germany*
[3]*Max-Planck-Institut für Kohlenforschung, Kaiser-Wilhelm-Platz 1, D-45470 Mülheim an der Ruhr, Germany*
[4]*Technical University of Denmark, Department of Chemical and Biochemical Engineering, Frederiksborgvej 399, 4000 Roskilde, Denmark*
[5]*Department of Physics and Astronomy, University College London, Gower Street, WC1E 6BT London, United Kingdom*

ABSTRACT

Comprehensive rotation-vibration line lists are presented for the two main isotopologues of methyl chloride, $^{12}CH_3^{35}Cl$ and $^{12}CH_3^{37}Cl$. The line lists, OYT-35 and OYT-37, are suitable for temperatures up to $T = 1200$ K and consider transitions with rotational excitation up to $J = 85$ in the wavenumber range $0 - 6400$ cm^{-1} (wavelengths $\lambda > 1.56\,\mu$m). Over 166 billion transitions among 10.2 million energy levels have been calculated variationally for each line list using a new empirically refined potential energy surface, determined by refining to 739 experimentally derived energy levels up to $J = 5$, and an established *ab initio* dipole moment surface. The OYT line lists show excellent agreement with newly measured high-temperature infrared absorption cross-sections, reproducing both strong and weak intensity features across the spectrum. The line lists are available from the ExoMol database and the CDS database.

Key words: molecular data – opacity – planets and satellites: atmospheres – stars: atmospheres – ISM: molecules.

1 INTRODUCTION

The recent interstellar detection of methyl chloride around the protostar IRAS 16293-2422 and in the coma of comet 67P/Churyumov–Gerasimenko (67P/C-G) (Fayolle et al. 2017) has undermined the possibility of CH$_3$Cl as a realistic biosignature gas in the search for life outside our Solar system (Segura et al. 2005; Seager, Bains & Hu 2013a,b). The fact that CH$_3$Cl can be formed abiotically in these environments, and possibly delivered by cometary impact to young planets, means it is now far more relevant in the context of newly formed rocky exoplanets. Consequently, there is renewed incentive for a comprehensive rotation-vibration line list of methyl chloride that is suitable for elevated temperatures.

Since 2012, the ExoMol database (Tennyson & Yurchenko 2012; Tennyson et al. 2016) has been generating molecular line lists and key spectroscopic data on a variety of small molecules deemed important for the characterization of hot astronomical atmospheres.

Notable applications utilizing ExoMol line lists include: the use of the 10to10 line list (Yurchenko & Tennyson 2014) to model methane in exoplanets (Beaulieu et al. 2011; Yurchenko et al. 2014; Tsiaras et al. 2018) and the bright T4.5 brown dwarf 2MASS 0559-14 (Yurchenko et al. 2014), and to assign lines in the near-infrared spectra of late T dwarfs (Canty et al. 2015) in combination with the ammonia BYTe line list (Yurchenko, Barber & Tennyson 2011); the early detection of water using the BT2 line list (Barber et al. 2006) in HD 189733b (Tinetti et al. 2007) and HD 209458b (Beaulieu et al. 2010); and the provisional identification of HCN in the atmosphere of super-Earth 55 Cancri e (Tsiaras et al. 2016) and TiO in the atmosphere of hot Jupiter WASP-76 b (Tsiaras et al. 2018). Conversely, a tentative detection of NaH in the atmosphere of a brown dwarf was ruled out using a line list for this molecule (Rivlin et al. 2015).

In this work, we present newly computed rotation-vibration line lists, named OYT-35 and OYT-37, for the two main isotopologues of methyl chloride, $^{12}CH_3^{35}Cl$ and $^{12}CH_3^{37}Cl$ (henceforth referred to as CH$_3^{35}$Cl and CH$_3^{37}$Cl). These line lists are validated against new high-temperature infrared (IR) absorption cross-sections measured at temperatures up to 500 °C. Methyl chloride

is the fourth pentatomic molecule to be considered within the EXOMOL framework (Tennyson & Yurchenko 2017) after the 10 to10 CH$_4$ line list (Yurchenko & Tennyson 2014), the line list of HNO$_3$ (Pavlyuchko, Yurchenko & Tennyson 2015), and the OY2T line list of SiH$_4$ (Owens et al. 2017). The OYT line lists are a continuation of our previous efforts where we constructed potential energy and dipole moment surfaces for CH$_3$Cl using state-of-the-art electronic structure theory (Owens et al. 2015, 2016). Variational nuclear motion calculations were used to rigorously evaluate these surfaces and they were shown to display excellent agreement with a range of experimental spectroscopic data. Notably, band shape and structure was well reproduced across the IR spectrum of CH$_3$Cl, even for weaker intensity features.

The paper is structured as follows: In Section 2, the theoretical approach and experimental setup are presented. This includes details on the empirical refinement of the potential energy surface (PES), the dipole moment surface (DMS) and intensity simulations, and the variational nuclear motion calculations. The OYT line lists are described in Section 3, where we look at the temperature-dependent partition functions of CH$_3$^{35}Cl and CH$_3$^{37}Cl, the format and temperature dependence of the OYT line lists, and comparisons with the HITRAN database and IR absorption cross-sections measured at temperatures up to 500 °C. We conclude in Section 4.

2 METHODS

2.1 PES refinement

The CBS-35$^{\text{HL}}$ PES (Owens et al. 2015) utilized in this work is based on extensive, high-level *ab initio* calculations. Despite reproducing the fundamentals with a root-mean-square (rms) error of 0.75 cm^{-1}, orders-of-magnitude improvements in the accuracy of the predicted transition frequencies can be obtained through empirical refinement of the PES. Improved energy levels also result in better wavefunctions and more reliable intensities. Since refinement is computationally intensive, the PES was only refined to CH$_3$^{35}Cl experimental term values, which is the main isotopologue. As we will see in Section 3, the resultant refined PES is still suitable for CH$_3$^{37}Cl.

The refinement was performed using an efficient least-squares fitting procedure (Yurchenko et al. 2011) implemented in the nuclear motion program TROVE (Yurchenko, Thiel & Jensen 2007). To make the procedure more computationally tractable for CH$_3$Cl, the number of expansion parameters of the CBS-35$^{\text{HL}}$ PES was carefully reduced from 414 to 188 without significant loss in accuracy. Of the 188 parameters, only 33 were eventually varied in the refinement. A total of 739 experimental term values up to $J = 5$ were used and this included 52 vibrational $J = 0$ band centres taken from Rothman et al. (2013), Nikitin, Champion & Bürger (2005), Duncan & Law (1990), Law (1999), and Bray et al. (2011). All $J > 0$ energies were taken from the HITRAN2012 database (Rothman et al. 2013) apart from the pure rotational energies of Nikitin & Champion (2005). Experimental energy levels from HITRAN are fairly robust as they are usually derived from numerous observed transitions, unlike for example, so-called dark states which are harder to determine. In particular, we had difficulty refining to the $2\nu_5(E)$, $2\nu_3 + \nu_5(E)$, and $3\nu_6(A_1)$ $J = 0$ states in the range ≈2895–3060 cm^{-1} from Bray et al. (2011) and their weights in the refinement were subsequently reduced to lessen their influence on the final PES. Pure rotational energy levels had the largest weights, while term values from HITRAN were weighted two orders-of-magnitude smaller. The remaining $J = 0$ energy levels not present in HITRAN, i.e. those from
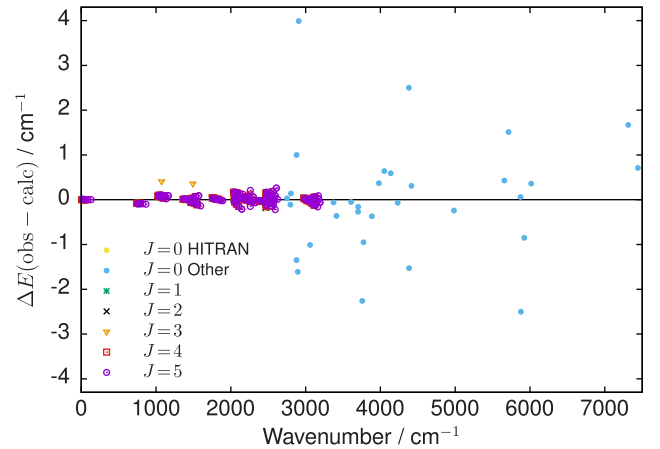

Figure 1. Fitting residuals, $\Delta E(\text{obs}-\text{calc}) = E_{\text{obs}} - E_{\text{calc}}$, of the 739 energy levels used in the PES refinement.

Duncan & Law (1990) and Law (1999), were given an order-of-magnitude smaller weights. Relative weighting is more important in the refinement than the absolute values since the weights are normalized (see Yurchenko et al. 2011 for further details).

Fig. 1 displays the results of the refinement through the fitting residuals $\Delta E(\text{obs}-\text{calc}) = E_{\text{obs}} - E_{\text{calc}}$, where E_{obs} and E_{calc} are the observed and calculated energies, respectively. The rms error for the 706 term values from HITRAN2012 is 0.072 cm^{-1} and this level of accuracy extends across all J. The remaining 33 $J = 0$ wavenumbers possess much larger residual errors and although this is partly due to the weighting, in certain cases we would have expected better agreement at lower energies. We therefore believe that the accuracy of some of the experimentally determined $J = 0$ levels can be improved. Unfortunately, we were unable to incorporate new data from the latest HITRAN2016 (Gordon et al. 2017) release, predominantly involving analysis of the 1900–2600 cm^{-1} spectral region (Nikitin, Dmitrieva & Gordon 2016), because the refinement was completed before this became available to us.

It should be noted that the accuracy of the refined PES can only be guaranteed with the exact computational setup used in this study. This is to be expected in theoretical line list production using programs that do not treat the kinetic energy operator exactly, e.g. TROVE. The refined PES is not recommended for future use but is provided in the supplementary material along with a FORTRAN routine to construct it.

2.2 DMS and line intensities

The electric DMS used in this work was generated at the CCSD(T)/aug-cc-pVQZ(+d for Cl) level of theory and the reader is referred to Owens et al. (2016) for a detailed description and evaluation of this surface. Absolute absorption intensities were simulated using the expression,

$$I(f \leftarrow i) = \frac{A_{if}}{8\pi c} g_{\text{ns}}(2J_f + 1) \frac{\exp(-E_i/kT)}{Q(T)\nu_{if}^2}$$

$$\times \left[1 - \exp\left(-\frac{hc\nu_{if}}{kT}\right) \right], \tag{1}$$

where A_{if} is the Einstein-A coefficient of a transition with wavenumber ν_{if} (in cm^{-1}) between an initial state with energy E_i and a final state with rotational quantum number J_f. Here, k is the Boltzmann constant, h is the Planck constant, c is the speed of light, and T

is the absolute temperature. The nuclear spin statistical weights of both isotopologues are $g_{ns} = \{16, 16, 16\}$ for states of symmetry $\{A_1, A_2, E\}$, respectively, and $Q(T)$ is the temperature-dependent partition function. Transitions follow the symmetry selection rules $A_1 \leftrightarrow A_2$, $E \leftrightarrow E$; and the standard rotational selection rules, $J' - J'' = 0, \pm 1$, $J' + J'' \neq 0$; where $'$ and $''$ denote the upper and lower state, respectively. All spectral simulations were carried out with the EXOCROSS code (Yurchenko, Al-Refaie & Tennyson 2018).

2.3 Variational calculations

Variational calculations were performed with TROVE, whose methodology has been well documented (Yurchenko et al. 2007; Yurchenko et al. 2009; Yachmenev & Yurchenko 2015; Tennyson & Yurchenko 2017; Yurchenko, Yachmenev & Ovsyannikov 2017). Since rovibrational computations on CH_3Cl have previously been reported (Owens et al. 2015, 2016), we describe only the key details relevant for this work.

An automatic differentiation method (Yachmenev & Yurchenko 2015) was used to construct the rovibrational Hamiltonian, which was represented as a power series expansion around the equilibrium geometry in terms of nine, curvilinear internal coordinates. The kinetic and potential energy operators were both truncated at sixth order. Atomic mass values were used throughout. The symmetrized vibrational basis set was generated using a multi-step contraction scheme (Yurchenko et al. 2017) and the size was controlled by the polyad number

$$P = 2(n_1 + n_2 + n_3 + n_4) + n_5 + n_6 + n_7 + n_8 + n_9 \leq P_{max}.$$
(2)

The quantum numbers n_k for $k = 1, \ldots, 9$ correspond to the primitive basis functions ϕ_{n_k}, which are determined by solving one-dimensional Schrödinger equations for each kth vibrational mode using the Numerov–Cooley method (Noumerov 1924; Cooley 1961). Multiplication with symmetrized rigid-rotor eigenfunctions $|J, K, m, \tau_{rot}\rangle$ gives the final basis set for $J > 0$ calculations. The quantum numbers K and m are the projections (in units of $\hbar$) of $\hat{J}$ on to the molecule-fixed z axis and the laboratory-fixed Z axis, respectively, while τ_{rot} determines the rotational parity as $(-1)^{\tau_{rot}}$.

Initially, $J = 0$ calculations were done with $P_{max} = 12$, which resulted in 49 076 vibrational basis functions with energies up to $hc \cdot 20\,600\,cm^{-1}$. With such a large basis set, describing rotational excitation quickly becomes computationally intractable and it was therefore necessary to reduce the number of basis functions. This was done using a basis set truncation procedure based on the vibrational transition moments. These are relatively inexpensive to compute in TROVE and such a scheme was previously employed when generating a comprehensive line list for SiH_4 (Owens et al. 2017). All possible transition moments were calculated for a lower state energy threshold of $hc \cdot 8000\,cm^{-1}$ (same as for the OYT line list intensity calculations), from which vibrational band intensities were estimated at an elevated temperature, e.g. 1500 K. For each $J = 0$ energy level, and thus each basis function, a band intensity value was assigned which was simply the largest value computed for that state. The vibrational basis set was then reduced by removing basis functions, and energy levels, above $hc \cdot 8000\,cm^{-1}$ with band intensity values smaller than $3 \times 10^{-22}\,cm\,molecule^{-1}$. This is around three orders-of-magnitude smaller than the largest computed value and was chosen primarily for computational reasons. The final pruned basis sets contained 2158 and 2156 vibrational basis functions with energies up to $hc \cdot 10\,400\,cm^{-1}$ for $CH_3{}^{35}Cl$ and

Table 1. Observed vibrational band centres ν (in cm^{-1}) from Nikitin et al. (2005) and Bray et al. (2011) used in the empirical basis set correction of the OYT line lists.

Mode	Sym.	ν ($CH_3{}^{35}Cl$)	ν ($CH_3{}^{37}Cl$)
ν_3	A_1	732.84	727.03
ν_6	E	1018.07	1017.68
ν_2	A_1	1354.88	1354.69
ν_5	E	1452.18	1452.16
$2\nu_3$	A_1	1456.76	1445.35
$\nu_3 + \nu_6$	E	1745.37	1739.24
$2\nu_6$	A_1	2029.38	2028.59
$2\nu_6$	E	2038.33	2037.56
$\nu_2 + \nu_3$	A_1	2080.54	2074.45
$3\nu_3$	A_1	2171.89	2155.12
$\nu_3 + \nu_5$	E	2182.57	2176.75
$\nu_2 + \nu_6$	E	2367.72	2367.14
$\nu_5 + \nu_6$	E	2461.65	2461.48
$2\nu_3 + \nu_6$	E	2463.82	2451.90
$\nu_5 + \nu_6$	A_1	2464.90	2464.47
$\nu_5 + \nu_6$	A_2	2467.67	2467.25
ν_1	A_1	2967.77	2967.75
ν_4	E	3037.14	3036.75
$3\nu_6$	E	3045.02	3044.14

$CH_3{}^{37}Cl$, respectively. They were multiplied in the usual manner with symmetrized rigid-rotor functions for $J > 0$ calculations. Naturally, by using this truncation procedure we will lose information on weaker lines involving states above $hc \cdot 8000\,cm^{-1}$ and without more rigorous calculations the exact effects are hard to quantify. Predicted rovibrational energies are also affected, however, we have compensated for this error to some extent by refining the PES with the pruned basis set.

The OYT line lists were computed with a lower state energy threshold of $hc \cdot 8000\,cm^{-1}$ and considered transitions up to $J = 85$ in the 0–6400 cm^{-1} range. The accuracy of the line lists was further improved by performing an empirical basis set correction (Yurchenko et al. 2009), which involves a shift of the vibrational band centres to better match experiment. For both isotopologues of CH_3Cl, we replaced 16 band centres up to 2500 cm^{-1} with values from Nikitin et al. (2005) and three band centres around the 3000 cm^{-1} region with values from Bray et al. (2011) (see Table 1).

2.4 Experimental setup

Mid IR CH_3Cl absorption measurements were carried out in the 600–6000 cm^{-1} region for temperatures in the range 22–500 °C (295.15–773.15 K) at a pressure of about 1 bar using a quartz flow gas cell as previously described in Grosch et al. (2013). Full details on the optical setup and raw data analysis can be found in Barton et al. (2015). Measurements used an Agilent 660 spectrometer with 0.09–2 cm^{-1} spectral resolution and a linearized broad-band mercury cadmium telluride (MCT) detector. The spectra were calculated from the measured interferograms using triangular apodization functions. The Lambert–Beer law was used for all absorption spectral calculations.

Pressurized CH_3Cl (99.8 per cent) from Air Liquide was diluted with N_2 (99.998 per cent) to obtain a CH_3Cl concentration in N_2 at the few vol per cent level. The CH_3Cl and N_2 flows were controlled with high-end mass-flow controllers (MFC). The actual CH_3Cl concentrations have been calculated based on known CH_3Cl and N_2

Table 2. Extract from the .states file of the OYT-35 line list.

n	$\tilde{E}$	g_{tot}	J	Γ_{tot}	n_1	n_2	n_3	n_4	n_5	n_6	n_7	n_8	n_9	Γ_{vib}	J	K	τ_{rot}	Γ_{rot}	$|C_i|^2$
1	0.000000	16	0	1	0	0	0	0	0	0	0	0	0	1	0	0	0	1	0.92
2	732.842200	16	0	1	1	0	0	0	0	0	0	0	0	1	0	0	0	1	0.89
3	1354.881100	16	0	1	0	0	0	0	0	1	0	0	0	1	0	0	0	1	0.29
4	1456.762600	16	0	1	2	0	0	0	0	0	0	0	0	1	0	0	0	1	0.85
5	2029.375300	16	0	1	0	0	0	0	0	0	2	0	0	1	0	0	0	1	0.13
6	2080.535700	16	0	1	1	0	0	0	0	1	0	0	0	1	0	0	0	1	0.26
7	2171.887500	16	0	1	3	0	0	0	0	0	0	0	0	1	0	0	0	1	0.80
8	2464.902500	16	0	1	0	0	0	0	0	0	1	0	1	1	0	0	0	1	0.22
9	2694.257786	16	0	1	0	0	0	0	1	1	0	0	0	1	0	0	0	1	0.18
10	2751.022753	16	0	1	1	0	0	0	0	0	2	0	0	1	0	0	0	1	0.12

n: State counting number;
$\tilde{E}$: Term value (in cm^{-1});
g_{tot}: Total degeneracy;
J: Rotational quantum number;
Γ_{tot}: Total symmetry in $\boldsymbol{C}_{3v}(M)$ (1 is A_1, 2 is A_2, 3 is E);
n_1-n_9: TROVE vibrational quantum numbers;
Γ_{vib}: Symmetry of the vibrational contribution in $\boldsymbol{C}_{3v}(M)$;
J: Rotational quantum number (same as column 4);
K: Rotational quantum number, projection of J onto molecule-fixed z axis;
τ_{rot}: Rotational parity (0 or 1);
Γ_{rot}: Symmetry of the rotational contribution in $\boldsymbol{C}_{3v}(M)$;
$|C_i^2|$: Largest coefficient used in the assignment.

flows (defined by the MFC) and were in the 1–7 vol per cent range. As a check of our experimental setup, measured spectra at 25 °C (resolution of 0.09 cm^{-1}) were compared with experimental data from the PNNL database (Sharpe et al. 2004), which employs a similar class Fourier Transform Infrared spectrometer in their measurements. The obtained results showed very good agreement with the PNNL database. Because CH$_3$Cl absorption features are relatively broad compared to a resolution of 0.09 cm^{-1}, most experiments were carried out with 0.5 cm^{-1} resolution to achieve better signal-to-noise ratio and measurement time. Experimental cross-sections of CH$_3$Cl in the region 600–6000 cm^{-1} are provided as supplementary material. This includes measurements for temperatures of 25, 300, 400, and 500 °C at a pressure of about 1 bar and resolution of 0.5 cm^{-1}.

The CH$_3$Cl IR absorption cross-sections are relatively low in the mid IR ($\approx 2.5 \times 10^{-20}$ cm^2/molecule). In practical applications these measurements are quite complicated because of possible spectral interferences with H$_2$O, CO$_2$, and H$_x$C$_y$. In general, relatively long (few metres) absorption path lengths are required for CH$_3$Cl measurements at the ppm-level but these difficulties can be overcome, for example, by employing a different spectral range. Molecules often possess relatively large absorption cross-sections below 200 nm, meaning the path length can be significantly reduced when measuring far ultraviolet (UV) or vacuum ultraviolet (VUV) spectra.

3 RESULTS

3.1 OYT line list format

The EXOMOL data structure has been adopted for the OYT line lists and a detailed description with illustrative examples can be found in Tennyson et al. (2016). The .states file (see Table 2) includes all the computed rovibrational energies (in cm^{-1}), with each energy level possessing a unique state counting number, symmetry and quantum number labelling, and the contribution $|C_i|^2$ from the largest eigen-coefficient used to assign the rovibrational state.

Table 3. Extract from the .trans file for the 0–100 cm^{-1} window of the OYT-35 line list.

f	i	A_{if}
9719527	9719368	1.1303e−11
9719740	9719588	2.2242e−17
9720687	9910074	2.1978e−16
9722798	9532161	1.8676e−21
97590	70456	2.4642e−07
97911	129246	2.7454e−15
98086	129430	2.1372e−11
98104	129459	5.3801e−12
981067	1101382	1.3658e−14
981676	913317	4.0655e−10

f: Upper state ID; i: Lower state ID;
A_{if}: Einstein-A coefficient (in s^{-1}).

The .trans files are split into 100 cm^{-1} frequency bins for handling purposes and contain all computed transitions with upper and lower state ID labels and Einstein-A coefficients, as shown in Table 3.

The TROVE (local mode) vibrational quantum numbers $n_1, \ldots, n_9$ can be related to the normal mode quantum numbers $v_1, \ldots v_6$ as follows:

$$v_3 = n_1, \quad \text{CCl} - \text{stretch},$$
$$v_1 + v_4 = n_2 + n_3 + n_4, \quad \text{CH} - \text{stretch},$$
$$v_2 + v_5 = n_5 + n_6 + n_7, \quad \text{CH}_3 - \text{bend},$$
$$v_6 = n_8 + n_9, \quad \text{CH}_3 - \text{rock}.$$

Due to the complicated three-step contraction scheme used to construct the symmetrized rovibrational basis set (Yurchenko et al. 2017), the connection with the primitive basis functions and the assignment based on the largest contribution from them is not straightforward. Therefore, especially in the case of small values of $|C_i|^2$, the assignment should only be considered as indicative.

In total, over 334 billion transitions have been computed and this is one of the largest data sets produced by the EXOMOL project to date. Although essential for the correct modelling of opacity at elevated temperatures (Yurchenko et al. 2014), handling such a huge number of lines is cumbersome and a more practical solution is to represent the OYT line lists in a more compact form such as the superlines format (Rey et al. 2016; Yurchenko et al. 2017), which is implemented in the EXOCROSS program (Yurchenko et al. 2018). To this end, we have generated a set of temperature-dependent superlines on a non-uniform grid with a constant resolving power of $R = \tilde{\nu}/\Delta\tilde{\nu} = 1\,000\,000$ (Yurchenko et al. 2017) for the 10–6400 cm^{-1} region and a uniform grid of 0.00001 cm^{-1} for 0-10 cm^{-1}, resulting in 7 461 473 grid points. Superlines are histograms of the absorption intensities (cm molecule^{-1}) distributed over this range. Each superline k is represented by the line position $\tilde{\nu}_k$ centred at the kth bin and the intensity $I_k(T)$ constructed from a sum of intensities $I_{fi}(T)$ of all transitions $f \leftarrow i$ within this bin. As part of the OYT line list package, superlines have been produced for $T = 300$, 400, ..., 1100, 1200 K. Each superline $[\tilde{\nu}_k, I_{fi}(T)]$ can be broadened in the standard way to produce pressure-dependent cross-sections with the advantage of a much smaller number of transitions, and a significantly reduced (by two to three orders-of-magnitude) computational cost.

Over 166 billion (166 279 320 228) transitions between 10.2 million (10 176 406) energy levels are contained in the OYT-35 line list, while the OYT-37 line list has 168 billion transitions (168 039 551 516) involving 10.2 million (10 187 780) states. Fig. 2 displays the distribution of lines and energies of the OYT-35 line list as a function of J. The largest number of transitions occurs around $J = 32$–33 before slowly and smoothly decreasing. For our computational setup, e.g. a lower state energy threshold of $hc \cdot 8000$ cm^{-1}, wavenumber range of 6400 cm^{-1}, pruned rovibrational basis set, etc., it is apparent that we have not calculated all possible transitions, which would require calculations up to approximately $J = 100$. Regarding the number of energy levels the decline after $J = 42$ is a consequence of the upper state energy threshold of $hc \cdot 14\,400$ cm^{-1}.

3.2 Partition function of methyl chloride

The temperature-dependent partition function $Q(T)$ is required for intensity simulations and is defined as,

$$Q(T) = \sum_i g_i \exp\left(\frac{E_i}{kT}\right), \tag{3}$$

where $g_i = g_{ns}(2J_i + 1)$ is the degeneracy of a state i with energy E_i and rotational quantum number J_i. Fig. 3 plots the convergence of $Q(T)$ for CH$_3{}^{35}$Cl as a function of J for selected temperatures. This was done by summing over all calculated rovibrational energy levels of the OYT-35 line list. Although it is not shown, the same behaviour is exhibited for CH$_3{}^{37}$Cl. The partition function is converged to around 0.2 per cent at $T = 1200$ K. Our computed room temperature partition functions for CH$_3{}^{35}$Cl and CH$_3{}^{37}$Cl are $Q(296\,\mathrm{K}) = 57\,973.557$ and $Q(296\,\mathrm{K}) = 58\,931.092$, respectively, which are very close to the values from the HITRAN database (Gamache et al. 2017). The full partition function for both isotopologues has been computed on a 1 K grid between 70–1400 K and is given as supplementary material.

Since the OYT line lists have been calculated using a lower state energy threshold of $hc \cdot 8000$ cm^{-1}, it is instructive to look at the reduced partition function Q_{limit}, which only includes energy levels up to $hc \cdot 8000$ cm^{-1} in the summation of equation (3). For CH$_3{}^{35}$Cl,
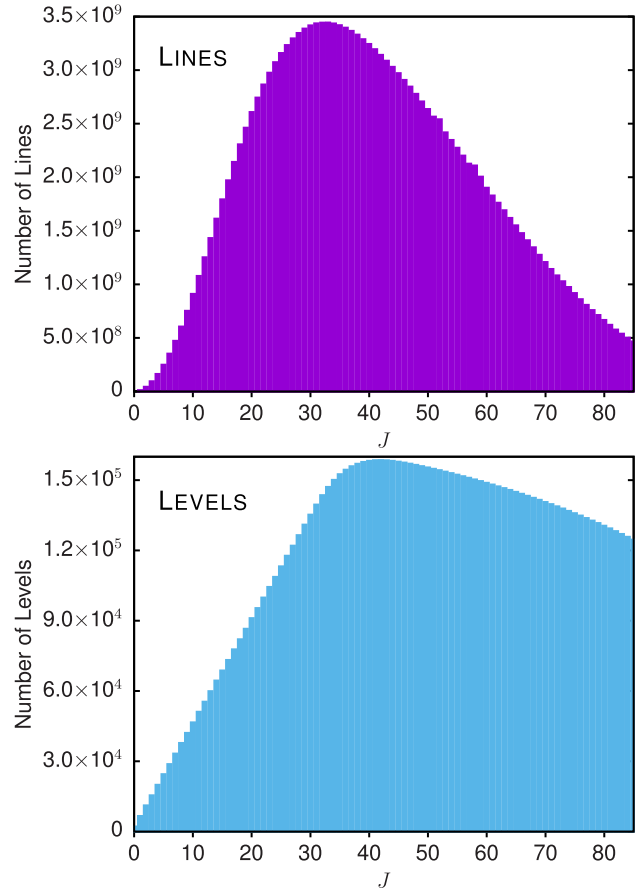

Figure 2. The total number of lines and energy levels in the OYT-35 line list for each value of the rotational quantum number J. Note that in the upper panel, a single J value counts transitions between $J \leftrightarrow J - 1$ and $J \leftrightarrow J$.
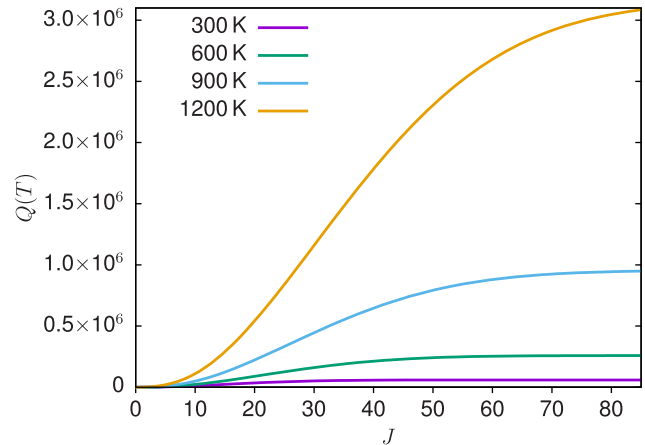

Figure 3. Convergence of the partition function $Q(T)$ of CH$_3{}^{35}$Cl with respect to the rotational quantum number J for select temperatures.

we have plotted the ratio Q_{limit}/Q with respect to temperature in Fig. 4. This measure allows the completeness of the OYT line lists to be evaluated. At $T = 1200$ K, the ratio $Q_{\mathrm{limit}}/Q = 0.96$ and this is recommended as a soft temperature limit to the OYT line lists. Above this temperature there will be a progressive loss of opacity
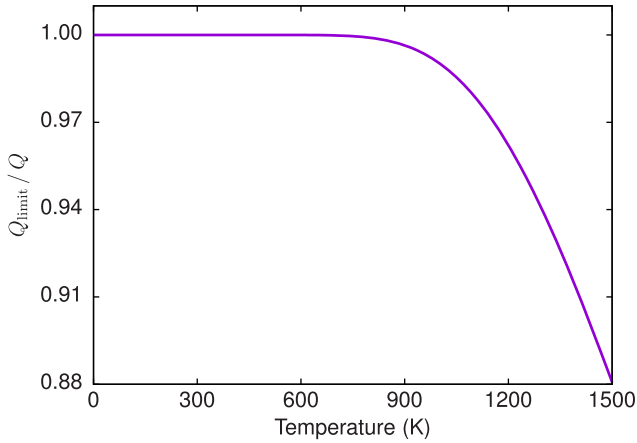
Figure 4. The ratio Q_{limit}/Q as a function of temperature; this provides a measure of completeness for the OYT line lists.
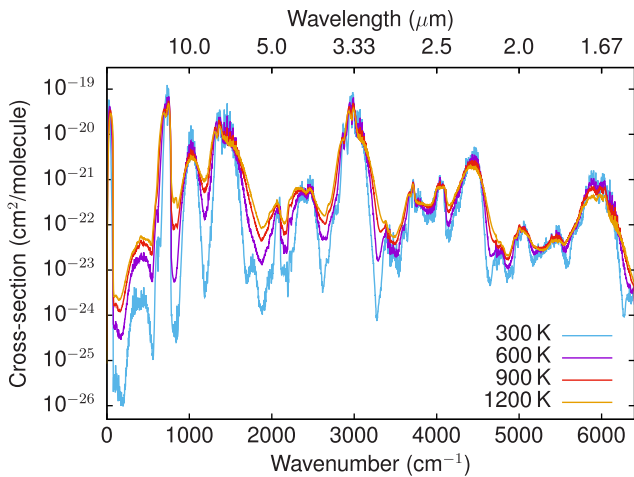

Figure 5. The OYT-35 line list temperature dependence: the spectrum becomes increasingly flat as the temperature is raised.

when using the OYT line lists but the missing contribution can be estimated through the ratio Q_{limit}/Q (Neale, Miller & Tennyson 1996).

3.3 Comparisons with the OYT line lists

In Fig. 5, integrated absorption cross-sections at a resolution of 1 cm^{-1} using a Gaussian profile with a half-width at half-maximum (hwhm) of 1 cm^{-1} have been simulated to illustrate the temperature dependence of the OYT-35 line list. As expected, weak intensities can increase several orders-of-magnitude in strength with rising temperature. This smoothing of the spectrum happens because of the increased population of vibrationally excited states, which causes the rotational band envelope to broaden. Although it is not shown, the OYT-37 line list exhibits identical behaviour.

An initial benchmark of the OYT line lists is shown in Fig. 6 and Fig. 7, where we have generated room temperature ($T = 296$ K) absolute line intensities and compared against all lines from the latest HITRAN database (Gordon et al. 2017). The OYT intensities have been scaled to natural abundance (0.748 937 for CH$_3$^{35}Cl and 0.239 491 for CH$_3$^{37}Cl), and because the rotational band of CH$_3$Cl
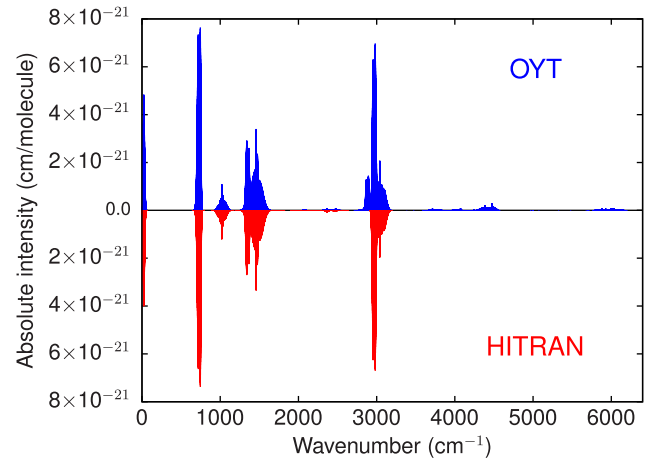

Figure 6. Comparison of the OYT line lists against all transitions from HITRAN2016 (Gordon et al. 2017). The OYT intensities have been scaled to natural abundance. The rotational band from HITRAN has been hyperfine 'unresolved' (see text).

is hyperfine resolved in HITRAN, we have 'unresolved' the experimental lines to compare with our calculations. As noted previously (Owens et al. 2016), the only noticeable band missing from HITRAN for wavenumbers below 3200 cm^{-1} appears to be the $2\nu_5$ band around 2880 cm^{-1}, which is not expected to be important for terrestrial atmospheric sensing. Otherwise the agreement is excellent and there are significant improvements compared to our previous efforts (Owens et al. 2015, 2016), particularly regarding line intensities which have benefited from improved variational calculations with an empirically refined PES.

Finally, in Fig. 8 and Fig. 9 we show comparisons with the newly measured high-temperature IR absorption cross-sections at 500 °C. The OYT spectra are of natural abundance and were simulated at a resolution of 0.1 cm^{-1} using a Voigt profile with a Lorentzian line width $\gamma_L = 0.3$ cm^{-1}. The agreement is extremely pleasing and all the key CH$_3$Cl spectral features are accounted for in the overview presented in Fig. 8. A closer inspection of the bands around 1400 cm^{-1}, 3000 cm^{-1}, and 4400 cm^{-1} in Fig. 9 provides further proof of the quality of the OYT line lists and confirms the validity of the computational procedure used to construct them.

4 CONCLUSION

Comprehensive rotation-vibration line lists for the two main isotopologues of methyl chloride, ^{12}CH$_3$^{35}Cl and ^{12}CH$_3$^{37}Cl, have been presented. The OYT-35 and OYT-37 line lists include transitions up to $J = 85$ in the 0–6400 cm^{-1} range. They are suitable for temperatures up to $T = 1200$ K. Applications above this temperature will lead to the loss of opacity and incorrect band shapes. Comparisons with newly measured high-temperature IR absorption cross-sections confirmed the accuracy and quality of the OYT line lists at elevated temperatures. Full line lists and superlines for both isotopologues are available from the EXOMOL database at www.exomol.com. The experimental cross sections reported in this work can be found in the CDS database at http://cdsarc.u-strasbg.fr together with thje superlines and .states files.

Possible extensions of the OYT line lists would be an increased lower state energy threshold and frequency range, and the treatment of higher rotational excitation. These issues are relatively straightforward to address, despite being computationally challenging, but
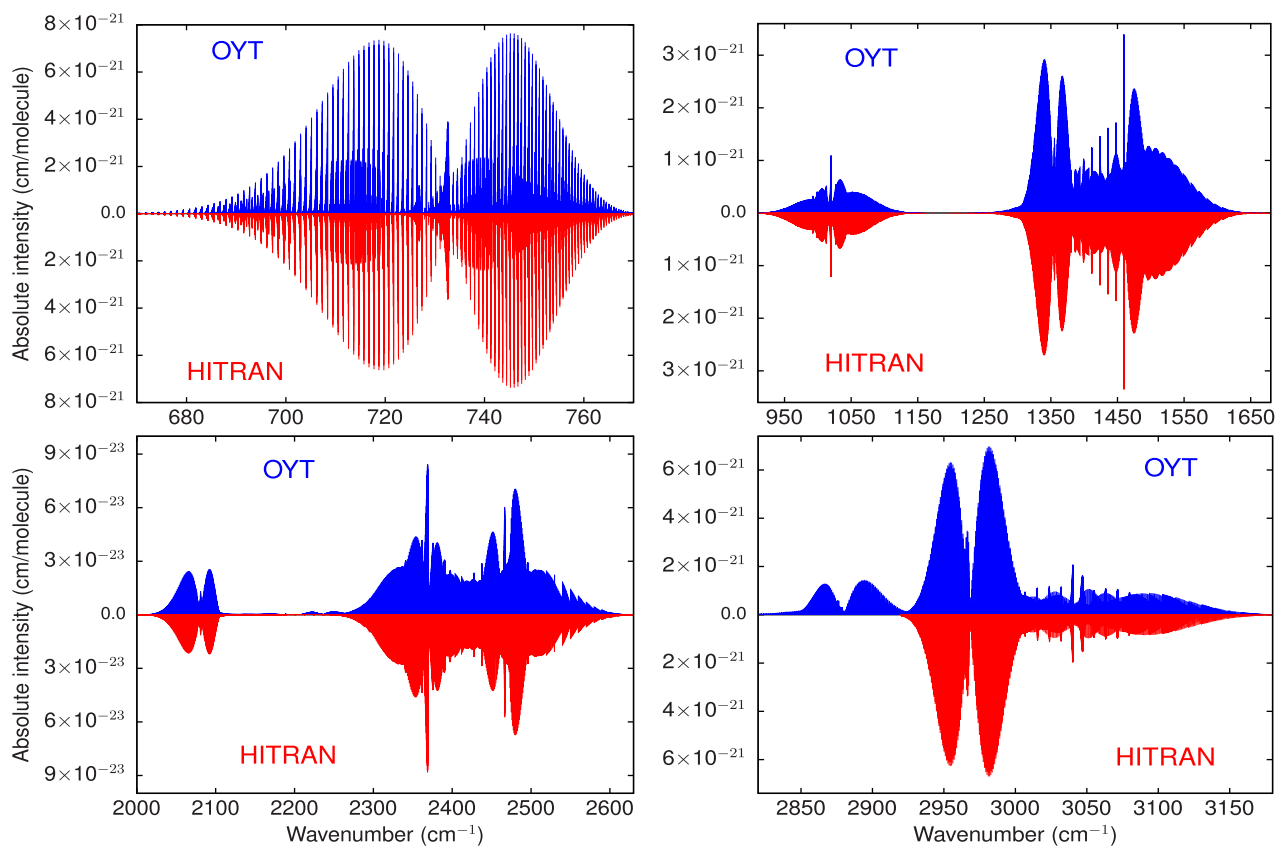
Figure 7. The OYT line lists compared with HITRAN2016 (Gordon et al. 2017). The OYT intensities have been scaled to natural abundance.
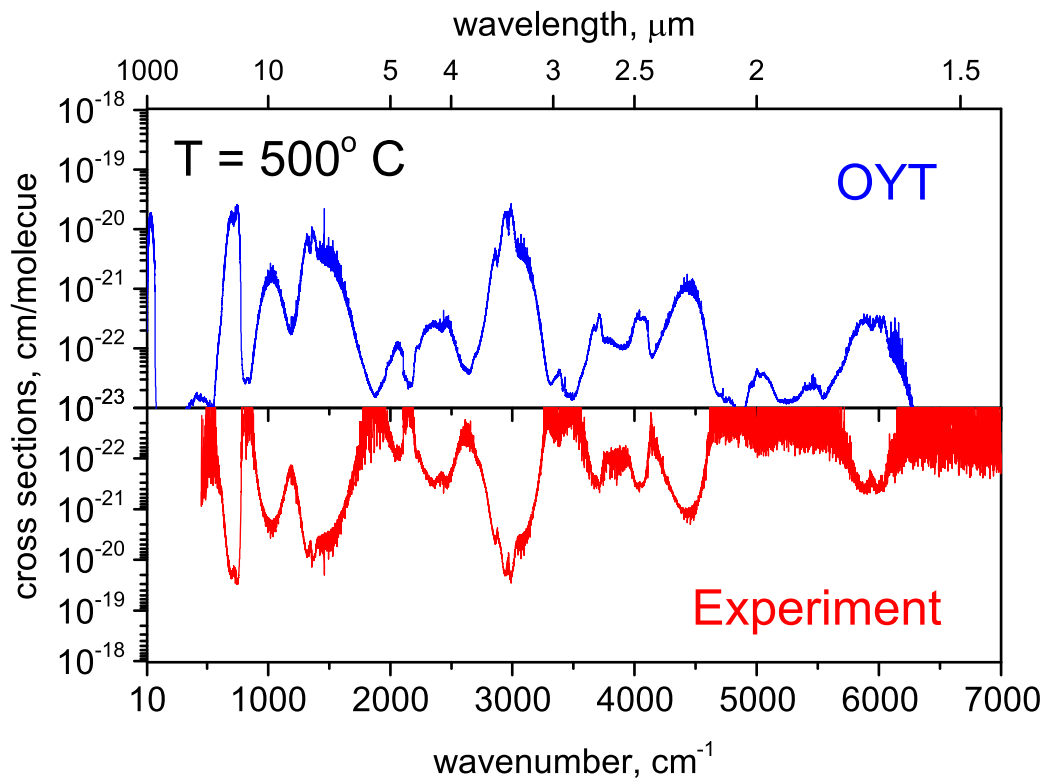

Figure 8. OYT absorption cross-sections simulated at 500 °C compared with the newly measured IR spectrum. Noise between 4700–7000 cm^{-1} is due to the light source and poor MCT detector sensitivity in that region.
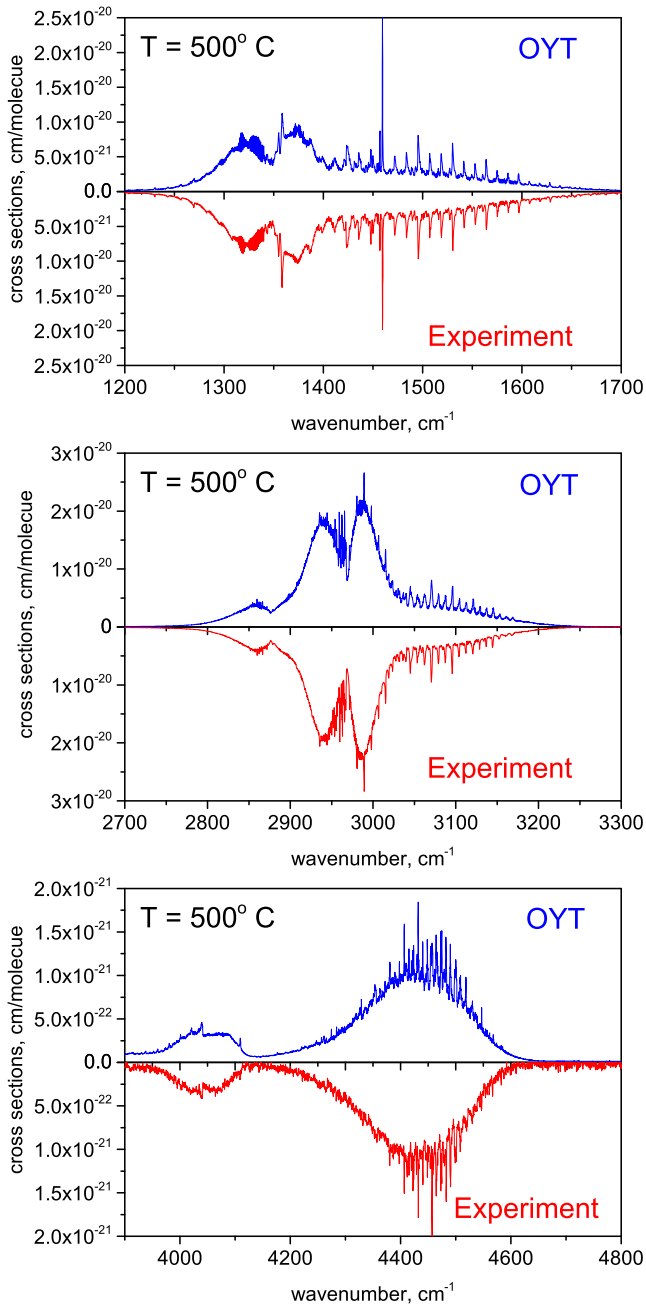
Figure 9. OYT absorption cross-sections simulated at 500 °C compared with the newly measured IR spectrum.

will only be done if there is a demand for such work. A complete set of normal mode quantum numbers v$_k$ for the OYT line lists would also be useful since these are routinely encountered in high-resolution spectroscopic applications and could be readily incorporated by updating the `.states` file. Any further updates will be made available on the EXOMOL website.

The completeness and accuracy of the OYT line lists should be adequate for modelling the absorption of methyl chloride in exoplanetary atmospheres. In principle, assuming the abundance of CH$_3$Cl is large enough for detection, transit spectroscopic observations combined with a proper atmospheric and radiative transfer model will be capable of this. For high-resolution detection techniques such as high-dispersion spectroscopy (Snellen 2014), the

OYT line positions may not be accurate enough. However, hybrid line lists, for example as recently reported for H$_3^+$ (Mizus et al. 2017), can overcome this issue by replacing the computed energy levels with experimentally derived ones, usually obtained with the measured active rotational-vibrational energy levels (MARVEL) procedure (Furtenbacher, Császár & Tennyson 2007; Furtenbacher & Császár 2012). Given the amount of experimental spectroscopic data available for CH$_3$Cl a hybrid line list like this could be constructed if necessary.

REFERENCES

Barber R. J., Tennyson J., Harris G. J., Tolchenov R. N., 2006, MNRAS, 368, 1087
Barton E. J., Yurchenko S. N., Tennyson J., Clausen S., Fateev A., 2015, J. Quant. Spectrosc. Radiat. Transf., 167, 126
Beaulieu J. P. et al., 2010, MNRAS, 409, 963
Beaulieu J. P. et al., 2011, ApJ, 731, 16
Bray C., Perrin A., Jacquemart D., Lacome N., 2011, J. Quant. Spectrosc. Radiat. Transf., 112, 2446
Canty J. I. et al., 2015, MNRAS, 450, 454
Cooley J. W., 1961, Math. Comput., 15, 363
Duncan J. L., Law M. M., 1990, J. Mol. Spectrosc., 140, 13
Fayolle E. C. et al., 2017, Nat. Astron., 1, 703
Furtenbacher T., Császár A. G., 2012, J. Quant. Spectrosc. Radiat. Transf., 113, 929
Furtenbacher T., Császár A. G., Tennyson J., 2007, J. Mol. Spectrosc., 245, 115
Gamache R. R., et al., 2017, J. Quant. Spectrosc. Radiat. Transf., 202, 70
Gordon I.E. et al., 2017, J. Quant. Spectrosc. Radiat. Transf., 203, 3
Grosch H., Fateev A., Nielsen K. L., Clausen S., 2013, J. Quant. Spectrosc. Radiat. Transf., 130, 392
Law M. M., 1999, J. Chem. Phys., 111, 10021
Mizus I. I., Alijah A., Zobov N. F., Lodi L., Kyuberis A. A., Yurchenko S. N., Tennyson J., Polyansky O. L., 2017, MNRAS, 468, 1717
Neale L., Miller S., Tennyson J., 1996, ApJ, 464, 516
Nikitin A., Champion J. P., 2005, J. Mol. Spectrosc., 230, 168
Nikitin A., Champion J. P., Bürger H., 2005, J. Mol. Spectrosc., 230, 174
Nikitin A. V., Dmitrieva T. A., Gordon I. E., 2016, J. Quant. Spectrosc. Radiat. Transf., 177, 49
Noumerov B. V., 1924, MNRAS, 84, 592
Owens A., Yurchenko S. N., Yachmenev A., Tennyson J., Thiel W., 2015, J. Chem. Phys., 142, 244306
Owens A., Yurchenko S. N., Yachmenev A., Tennyson J., Thiel W., 2016, J. Quant. Spectrosc. Radiat. Transf., 184, 100
Owens A., Yachmenev A., Thiel W., Tennyson J., Yurchenko S. N., 2017, MNRAS, 471, 5025

Pavlyuchko A. I., Yurchenko S. N., Tennyson J., 2015, MNRAS, 452, 1702

Rey M., Nikitin A. V., Babikov Y. L., Tyuterev V. G., 2016, J. Mol. Spectrosc., 327, 138

Rivlin T., Lodi L., Yurchenko S. N., Tennyson J., Le Roy R. J., 2015, MNRAS, 451, 5153

Rothman L. et al., 2013, J. Quant. Spectrosc. Radiat. Transf., 130, 4

Seager S., Bains W., Hu R., 2013a, ApJ, 775, 104

Seager S., Bains W., Hu R., 2013b, ApJ, 777, 95

Segura A., Kasting J. F., Meadows V., Cohen M., Scalo J., Crisp D., Butler R. A. H., Tinetti G., 2005, Astrobiology, 5, 706

Sharpe S. W., Johnson T. J., Sams R. L., Chu P. M., Rhoderick G. C., Johnson P. A., 2004, Appl. Spectrosc., 58, 1452

Snellen I., 2014, Phil. Trans. Royal Soc. London A, 372, 20130075

Tennyson J. et al., 2016, J. Mol. Spectrosc., 327, 73

Tennyson J., Yurchenko S. N., 2012, MNRAS, 425, 21

Tennyson J., Yurchenko S. N., 2017, Int. J. Quantum Chem., 117, 92

Tinetti G. et al., 2007, Nature, 448, 169

Tsiaras A. et al., 2016, ApJ, 820, 99

Tsiaras A. et al., 2018, AJ, 155, 156

Yachmenev A., Yurchenko S. N., 2015, J. Chem. Phys., 143, 014105

Yurchenko S. N., Tennyson J., 2014, MNRAS, 440, 1649

Yurchenko S. N., Thiel W., Jensen P., 2007, J. Mol. Spectrosc., 245, 126

Yurchenko S. N., Barber R. J., Yachmenev A., Thiel W., Jensen P., Tennyson J., 2009, J. Phys. Chem. A, 113, 11845

Yurchenko S. N., Barber R. J., Tennyson J., Thiel W., Jensen P., 2011, J. Mol. Spectrosc., 268, 123

Yurchenko S. N., Barber R. J., Tennyson J., 2011, MNRAS, 413, 1828

Yurchenko S. N., Tennyson J., Bailey J., Hollis M. D. J., Tinetti G., 2014, Proc. Natl. Acad. Sci. U.S.A., 111, 9379

Yurchenko S. N., Amundsen D. S., Tennyson J., Waldmann I. P., 2017, A&A, 605, A95

Yurchenko S. N., Yachmenev A., Ovsyannikov R. I., 2017, J. Chem. Theory Comput., 13, 4368

Yurchenko S. N., Al-Refaie A. F., Tennyson J., 2018, A&A, **614**, A131

SUPPORTING INFORMATION

Supplementary data are available at *MNRAS* online.

Please note: Oxford University Press is not responsible for the content or functionality of any supporting materials supplied by the authors. Any queries (other than missing material) should be directed to the corresponding author for the article.

This paper has been typeset from a TEX/LATEX file prepared by the author.